

COMPACT H II REGIONS: HYDROGEN RECOMBINATION AND OH MASER LINES

GUIDO GARAY, MARK J. REID, AND JAMES M. MORAN

Harvard-Smithsonian Center for Astrophysics

Received 1984 July 23; accepted 1984 August 27

ABSTRACT

Hydrogen recombination lines at 15 and 22 GHz and hydroxyl (OH) maser emission at 1.6 GHz have been mapped toward nine compact H II regions using the VLA. We find that all OH masers have radial velocities which are redshifted from the velocities of the H II regions as deduced from their hydrogen recombination lines. The majority of the maser spots appear projected onto the most compact H II region in a complex. These observations are inconsistent with models in which the masers form in an expanding, shocked shell, and they are explained most simply if the OH maser sources are part of a remnant envelope which is still collapsing toward the newly formed star.

Subject headings: interferometry — masers — nebulae: H II regions — shock waves — stars: formation

I. INTRODUCTION

Studies of regions of star formation at radio wavelengths have established that there is a close relationship between interstellar hydroxyl (OH) masers and compact H II regions (e.g., Mezger *et al.* 1967; Evans *et al.* 1979; Ho *et al.* 1983). Based on the VLBI observations of Moran *et al.* (1968) and subsequent interferometer work, Cook (1968), Baldwin, Harris, and Ryle (1973), and Elitzur and de Jong (1978) suggested that OH masers are located in a compressed shell between the shock and ionization fronts around compact H II regions. However, VLBI aperture synthesis observations of the OH maser emission toward the compact H II region W3(OH) do not support this shock model. Reid *et al.* (1980) found that the radial velocities of the OH masers in W3(OH) are redshifted with respect to the velocity of the underlying compact H II region. Because the masers are projected against the compact H II region, whose continuum emission is optically thick at the 1.6-GHz OH maser transition, they appear to be moving toward the compact H II region. Reid *et al.* (1980) suggest that the OH masers in W3(OH) are located in a remnant envelope which is still collapsing toward the recently formed star. Clearly, observations of other sources were needed to establish whether or not the situation in W3(OH) is typical.

To understand the dynamics of the masing region, it is essential to know the velocity of the underlying star. The velocity of the young star can be estimated by observations of recombination lines from the ionized circumstellar material. It is difficult to detect shifts of $\sim 5 \text{ km s}^{-1}$ from the OH emission with Br α observation in the infrared. Radio-frequency observations of recombination lines can provide higher spectral resolution. However, since the angular sizes of compact H II regions are typically a few arcseconds and their flux densities are typically about 1 Jy, an instrument having very high angular resolution and sensitivity is required. The Very Large Array (VLA) in its more compact configurations is an ideal instrument for studies of recombination lines in compact H II regions.

In this paper we report radio-frequency, recombination-line observations of nine complexes of compact H II regions associated with OH masers. The observed sources were selected from the list of regions of star formation compiled by Habing and Israel (1979) that have known compact and/or ultracompact H II regions and associated OH maser emission. There are

about 30 such regions on the list. We selected the nine regions that are observable from the VLA and that have compact H II regions with observed or predicted flux densities of greater than 1 Jy at 15 GHz, so that recombination-line studies were possible with integration times of less than a few hours.

The OH maser emission had been accurately (i.e., $< 1''$ uncertainty) mapped toward only two of the nine compact H II regions. The OH positions for the rest of the sources had been previously determined to accuracies of only $5''$, which is insufficient to define clearly a physical association of the compact H II and OH masers. In this paper we also report the positions of OH maser spots toward eight of the regions of star formation derived from spectral-line observations at the VLA, which have accuracies better than $0''.2$.

II. OBSERVATIONS

a) Hydrogen Recombination Lines

The observations were made at the Very Large Array (VLA) of the National Radio Astronomy Observatory,¹ using the D configuration in 1981 September and the C configuration in 1982 January. We observed nine H II region complexes associated with OH maser emission. The instrumental parameters are given in Table 1. Four sources were observed in the H76 α radio recombination line of hydrogen at 14.690 GHz (*U*-band, 2 cm wavelength), and six sources were observed in the H66 α transition at 22.364 GHz (*K* band, 1.35 cm wavelength).

In the D configuration the maximum baseline was ~ 1.0 km, providing an angular resolution of $6''$ and $4''$ at *U* and *K* band, respectively. In the C configuration the maximum baseline was ~ 3.0 km, giving a resolution of $\sim 2''$ at *K* band. We used a 12.5 MHz bandwidth with a channel separation of 0.391 MHz which gave a velocity resolution of 8.0 and 5.3 km s^{-1} at *U* and *K* band, respectively. VLA spectral-line observations were limited by computer capabilities to a total of 5120 correlator channels. For the *U*-band observations we chose a configuration of 25 antennas and 15 spectral channels, which provided a velocity coverage of 120 km s^{-1} ; for the *K*-band observations we used 18 antennas and 31 spectral channels, which

¹ The National Radio Astronomy Observatory is operated by Associated Universities, Inc., under contract with the National Science Foundation.

TABLE 1
INSTRUMENTAL PARAMETERS

H II REGION COMPLEX	PHASE TRACKING CENTER		OBSERVED FREQUENCY (GHz)	VLA CONFIGURATION	HPBW (")
	Right Ascension (1950)	Declination (1950)			
W3(OH)	02 ^h 23 ^m 16 ^s .5	61°38'58".0	22.4	C	1.8 × 1.3
	02 23 16.5	61 38 58.0	14.7	D	5.7 × 3.1
Sgr B2	17 44 10.6	-28 22 05.0	14.7	D	7.2 × 3.6
G10.6-0.4	18 07 30.8	-19 56 28.0	22.4	D	3.9 × 2.7
G19.6-0.2	18 24 50.9	-11 58 26.0	22.4	C	2.0 × 1.5
G20.1-0.1	18 25 23.0	-11 30 46.0	22.4	C	2.0 × 1.5
G34.3+0.2	18 50 46.2	01 11 12.7	22.4	C	1.7 × 1.7
W49S	19 07 58.3	09 00 05.0	14.7	D	4.4 × 4.0
G45.07+0.13	19 11 00.3	10 45 45.0	22.4	C	1.8 × 1.6
W51	19 21 23.1	14 25 00.0	14.7	D	4.1 × 3.9

provided a velocity coverage of 163 km s^{-1} . The VLA spectral-line system also provides a continuum channel which contains the average of the central 75% of the total available bandpass.

Total integration time for each source was ~ 90 minutes, obtained from 10 minute scans at different hour angles chosen to provide good (u, v)-plane coverage. Calibrator sources were observed for 4 minutes before and after every on-source scan to correct the amplitude and phase of the interferometer data for atmospheric and instrumental effects. The strong source 3C 84 was observed twice during each observing run for approximately 30 minutes for bandpass calibration. We used the spectral-line data-analysis procedures described by Rots (1981). Maps were made for each frequency channel by Fourier transformation of the interferometer data.

b) OH Emission

Spectral-line observations of OH masers were made in 1982 April with the VLA in the A configuration. The maximum baseline was ~ 35 km, providing a resolution of $\sim 1''.5$ at the rest frequency of 1665.4018 MHz. We used a bandwidth of 1.56 MHz with a channel separation of 6.1 KHz, which gave a velocity resolution of 1.1 km s^{-1} . The correlator was configured for 25 antennas and 15 spectral channels which provided a velocity coverage of 16.5 km s^{-1} . The observations consisted of 5 minute integrations on source, preceded and followed by 3 minute integrations on a nearby calibrator. Observations were made in right and left circular polarization. No bandpass calibration was necessary since a narrow bandwidth was used and the maser emission is much stronger than the continuum emission. Maps were made for each spectral channel by Fourier transformation of the interferometer data.

III. OBSERVATIONAL RESULTS

a) Continuum Emission

The continuum maps of the nine regions of star formation are shown in Figures 1 through 9. Usually several compact H II regions were detected within a star-forming region, which demonstrates the gregarious nature of these objects. The positions, flux densities, and sizes of individual compact H II regions within each complex are given in Table 2. Due to uncertainties in telescope gain at the high frequencies, the absolute flux densities have errors of 30%.

b) Hydrogen Recombination Lines

The recombination-line velocity, amplitude, and linewidth for each source were determined by simultaneously fitting a

Gaussian profile and a linear baseline to the spectrum obtained from the map data. The data and fitted profiles are shown in the insets of Figures 1 through 9. The derived parameters are listed in Table 3. We estimate that realistic 1σ errors are 1.0 km s^{-1} , 4.0 km s^{-1} , and 0.04 for the velocity, linewidth, and line-to-continuum ratio, respectively.

c) OH Maser Emission

The center velocity, position, polarization, and flux density of each OH maser feature are given in Table 4. The center velocity of an OH feature was determined by fitting a Gaussian profile to the spectral data at a given position in the map. The spectra are shown in Figure 10. Due to the limited spectral-line capability of the VLA at the time of our observations (see § II), some OH maser features fall outside the observed band and could not be mapped.

In Figures 2 to 9 we plot the OH positions (indicated by black dots) on the maps of associated compact H II regions. Errors in the absolute positions of the OH maser features are due mostly to uncertainties in the calibrator positions and to atmospheric irregularities, and those errors are $\sim 0''.2$. The relative positions of the OH features are much better determined and have 1σ errors of $\sim 0''.02$. In most of the regions, the OH maser spots are projected onto the face of a single compact H II region. To demonstrate this projection, we present in Figure 11 a composite picture of the spatial distribution of all the OH maser spots relative to their associated compact H II regions. All maser positions are measured with respect to the center of the associated H II region in units of the radius of the associated H II region. To investigate the radial density of OH masers, we performed an azimuthal summation of the data, as shown in Figure 12. Figure 12 shows the distribution of OH maser features as a function of its normalized distance from the center of the compact H II region. The abscissa intervals correspond to equal area increments so that the ordinate is proportional to the area density of OH features. This figure shows that $\sim \frac{2}{3}$ of the OH maser features are projected on the face of the H II region (i.e., at a distance less than the half-power radius of the H II region), and that there is an increase in the OH feature density toward the center of the compact H II region.

IV. DERIVED PARAMETERS

a) Compact H II Regions

The physical parameters derived for the H II regions were calculated assuming that the lines form in local thermodyna-

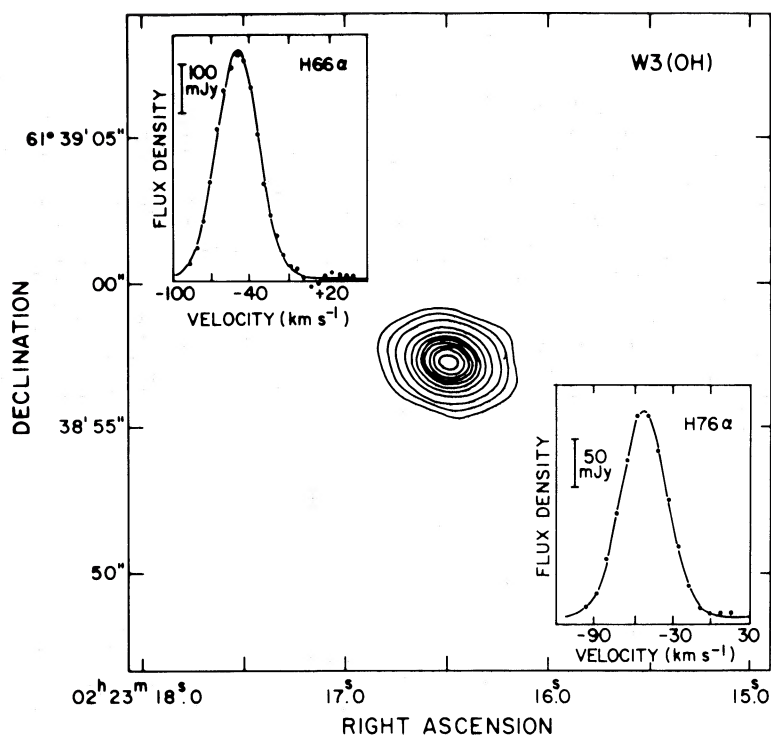


FIG. 1.—Continuum VLA map at 22.4 GHz of the compact H II region W3(OH). The contour levels are $-2, 2, 5, 10, 20, 30, 40, 50, 60, 70, 80,$ and 90 percent of the peak flux density of 2.9 Jy per beam. The H66 α and H76 α recombination-line profiles are shown in the upper-left and lower-right corners, respectively. Velocity axes are with respect to the local standard of rest.

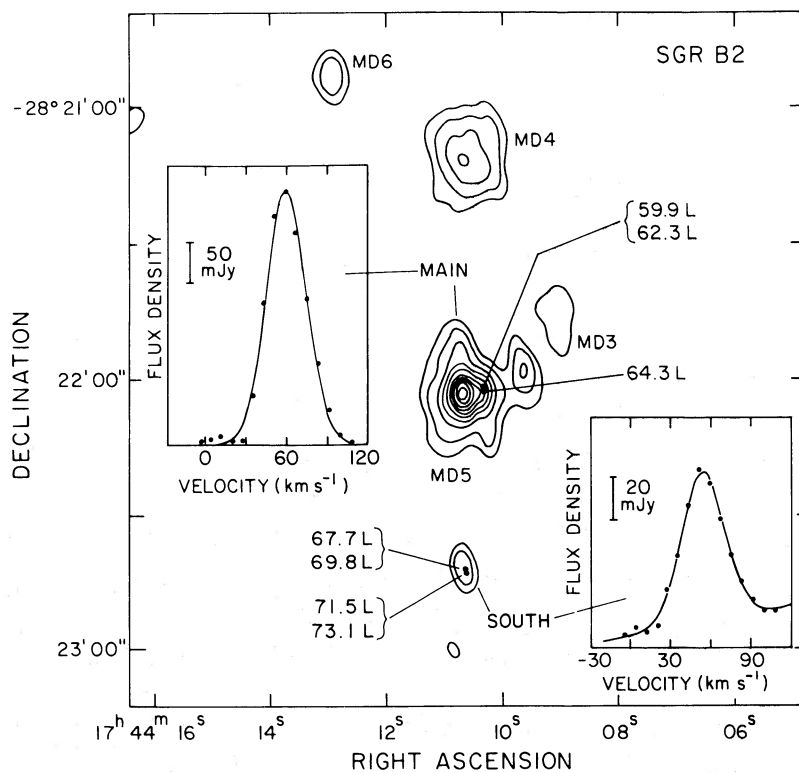


FIG. 2.—Continuum VLA map at 14.7 GHz of the Sgr B2 star-forming region. The contour levels are $-5, 5, 10, 20, 30, 40, 50, 60, 70, 80,$ and 90 percent of the peak flux density of 3.5 Jy per beam. The black dots indicate the position of the OH maser features, labeled by their LSR velocity and sense of circular polarization (R = RCP, L = LCP). The H76 α recombination-line profile of the Main and South components are shown in the upper-left and lower-right corners, respectively.

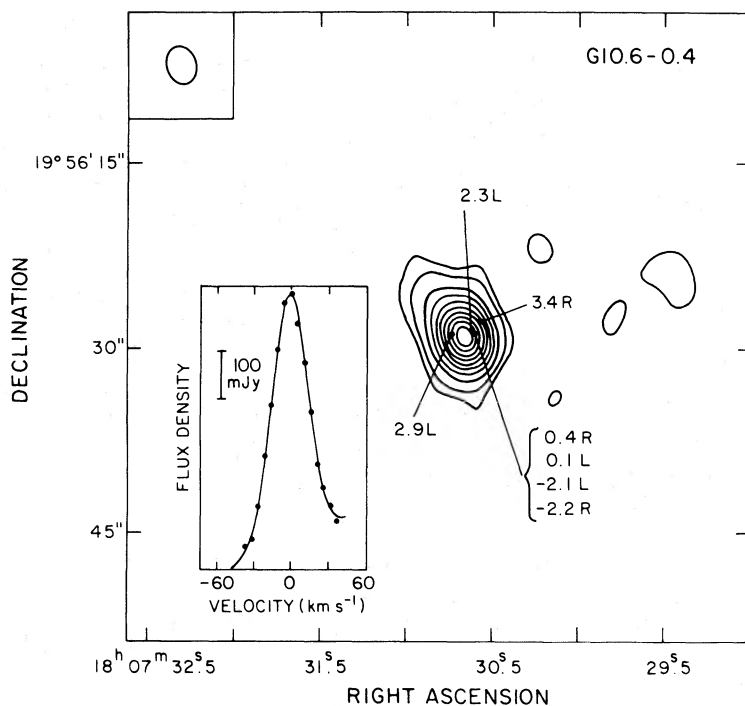


FIG. 3.—Continuum VLA map at 22.4 GHz of the G10.6–0.4 star-forming region. The contour levels are –5, 5, 10, 20, 30, 40, 50, 60, 70, 80, and 90 percent of the peak flux density of 2.1 Jy per beam. The black dots indicate the position of the OH maser features, labeled by their LSR velocity and sense of circular polarization (R = RCP, L = LCP). The H66 α recombination-line profile is shown in the lower-left corner. The VLA beam is shown in the upper-left corner.

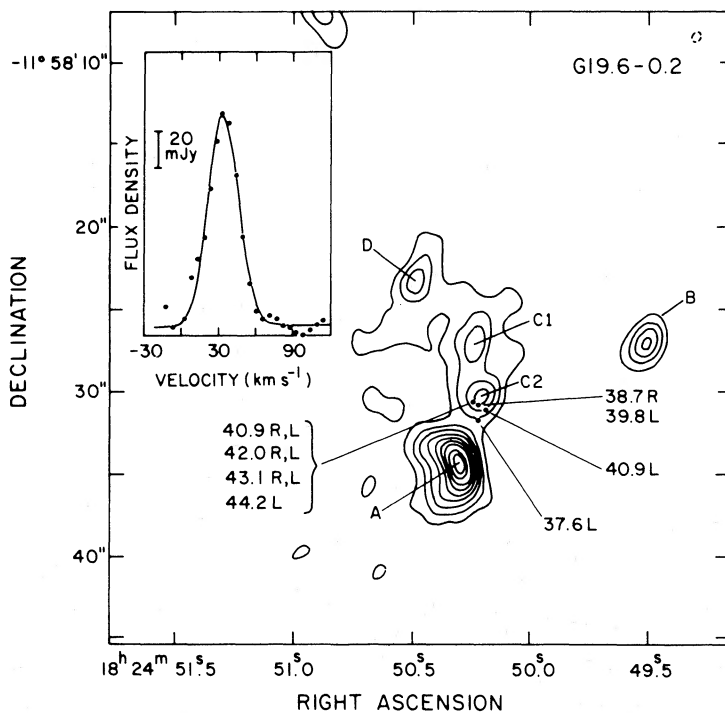


FIG. 4.—Continuum VLA map at 22.4 GHz of the G19.6–0.2 star-forming region. The contour levels are –10, 10, 20, 30, 40, 50, 60, 70, 80, and 90 percent of the peak flux density of 0.24 Jy per beam. The parameters of five distinct sources labeled A–D are given in Table 2. The black dots indicate the position of the OH maser features, labeled by their LSR velocity and sense of circular polarization (R = RCP, L = LCP). The H66 α recombination-line profile is shown in the upper-left corner.

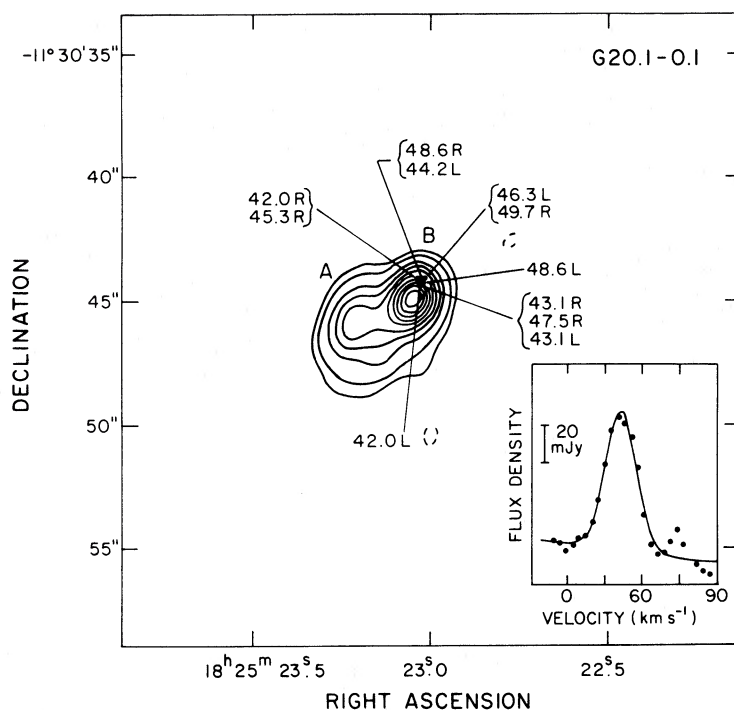


FIG. 5.—Continuum VLA map at 22.4 GHz of the G20.1–0.1 star-forming region. The contour levels are –5, 5, 10, 20, 30, 40, 50, 60, 70, 80, and 90 percent of the peak flux density of 0.36 Jy per beam. The black dots indicate the position of the OH maser features, labeled by their LSR velocity and sense of circular polarization (R = RCP, L = LCP). The H66 α recombination-line profile is shown in the lower-right corner.

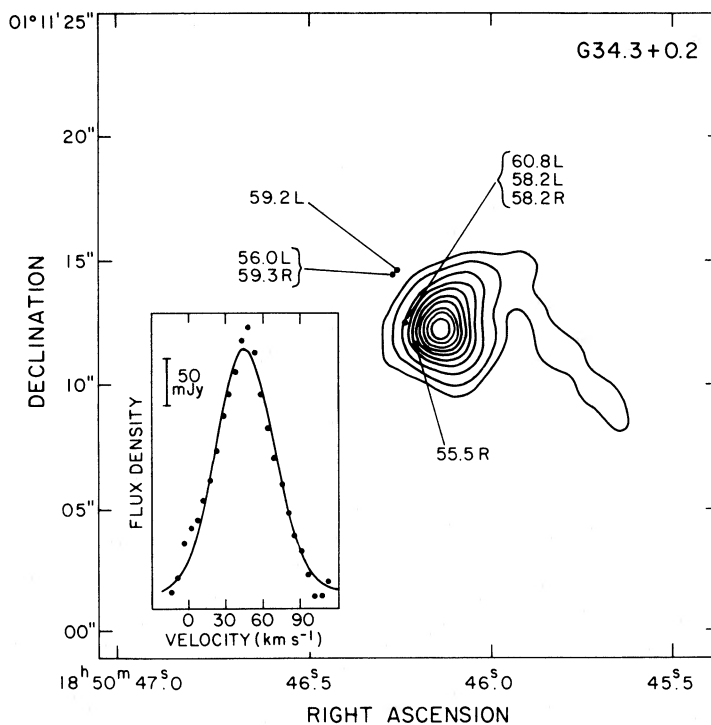


FIG. 6.—Continuum VLA map at 22.4 GHz of the G34.3+0.2 star-forming region. The contour levels are –5, 5, 10, 20, 30, 40, 50, 60, 70, 80, and 90 percent of the peak flux density of 1.8 Jy per beam. The black dots indicate the position of the OH maser features, labeled by their LSR velocity and sense of circular polarization (R = RCP, L = LCP). The H66 α recombination-line profile is shown in the lower-left corner.

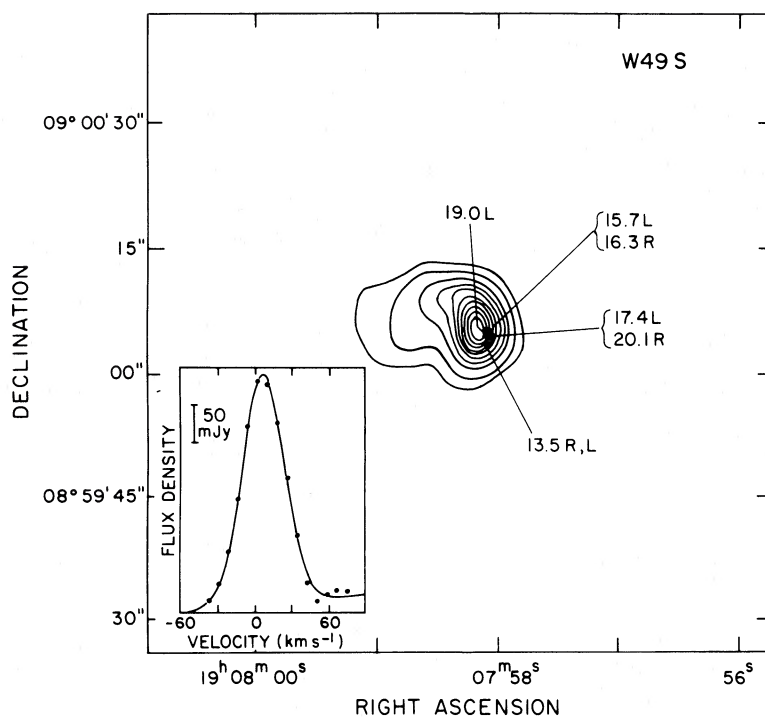


FIG. 7.—Continuum VLA map at 14.7 GHz of the W49S star-forming region. The contour levels are $-5, 5, 10, 20, 30, 40, 50, 60, 70, 80,$ and 90 percent of the peak flux density of 2.6 Jy per beam. The black dots indicate the position of the OH maser features, labeled by their LSR velocity and sense of circular polarization (R = RCP, L = LCP). The $H76\alpha$ recombination-line profile is shown in the lower-left corner.

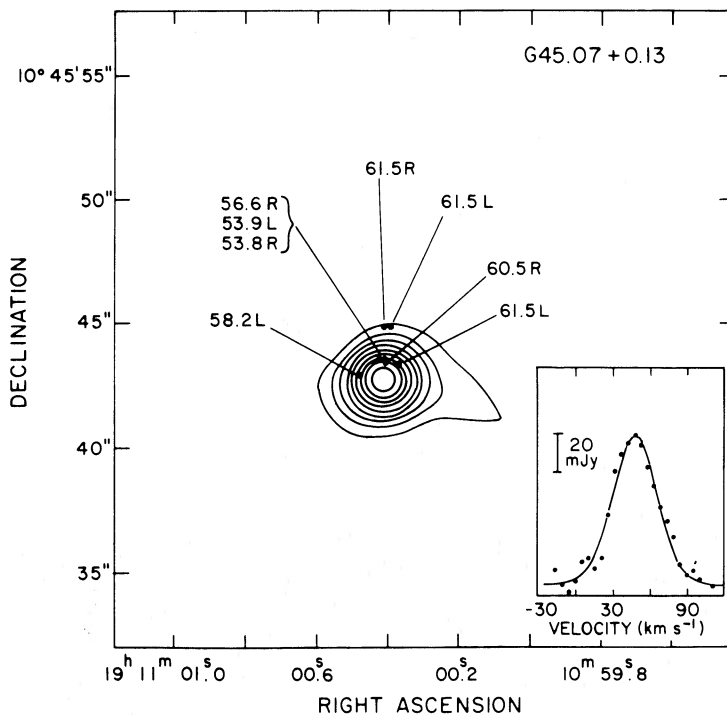


FIG. 8.—Continuum VLA map at 22.4 GHz of the G45.07+0.13 star-forming region. The contour levels are $-10, 10, 20, 30, 40, 50, 60, 70, 80,$ and 90 percent of the peak flux density of 0.53 Jy per beam. The black dots indicate the position of the OH maser features, labeled by their LSR velocity and sense of circular polarization (R = RCP, L = LCP). The $H66\alpha$ recombination-line profile is shown in the lower-right corner.

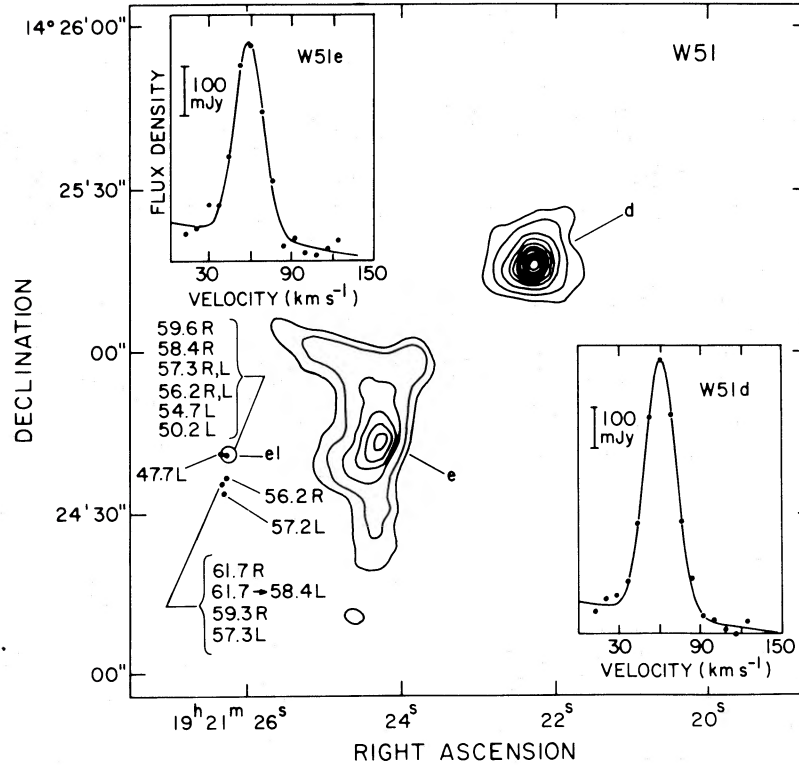


FIG. 9.—Continuum VLA map at 14.7 GHz of the W51 star-forming region. The contour levels are $-5, 10, 20, 30, 40, 50, 60, 70, 80,$ and 90 percent of the peak flux density of 3.5 Jy per beam. The black dots indicate the position of the OH maser features, labeled by their LSR velocity and sense of circular polarization (R = RCP, L = LCP). The H76 α recombination-line profile of the d and e components are shown in the lower-right and upper-left corners, respectively.

mic equilibrium, and that the lines are not affected by pressure broadening. Under these conditions, the electron temperature, T_e^* , can be expressed in terms of observables as (cf. Hughes and Viner 1976):

$$T_e^* = 6.37 \times 10^4 \left(\frac{v^2}{\Delta v_D} \right) \left(\frac{T_C}{T_L} \right) \left(\frac{E_L}{E_c} \right) \times \frac{1}{\ln(4.96 \times 10^{-2} T_e^{3/2} v^{-1})} \left(\frac{\tau_c}{e^{\tau_c} - 1} \right), \quad (1)$$

where T_L/T_C is the observed line-to-continuum ratio, Δv_D is the observed line width in kHz, v is the observing frequency in GHz, E_L/E_c is the line-to-continuum emission measure ratio, and τ_c is the continuum optical depth.

Provided the path lengths for continuum and line radiation are the same,

$$\frac{E_L}{E_c} = \frac{N(\text{H}^+)}{N(\text{H}^+) + N(\text{He}^+)}, \quad (2)$$

where $N(\text{H}^+)$ and $N(\text{He}^+)$ are number densities of ionized hydrogen and helium. In this paper we assume a constant value for E_L/E_c of 0.90.

The compact H II regions we observed have emission measures of $\lesssim 10^9 \text{ cm}^{-6} \text{ pc}$ (assuming an electron temperature of 10^4 K) and thus would be expected to have an optical depth of unity at about $\lesssim 10$ GHz. Our observations at 5, 15, and 22 GHz verify this assumption and indicate that most of the compact H II regions have turnover frequencies below the observed line frequencies. Spectra of some of the compact H II

regions are shown in Figure 13. Typical continuum optical depths at the line frequencies are less than 0.3. Thus, the assumption of optically thin continuum emission is a reasonable approximation.

Pressure broadening may affect line profiles for compact H II regions that have high densities. The ratio of total line width, Δv_T , to the thermal line width, Δv_{th} , for hydrogen recombination lines arising from ionized gas with electron density N_e , electron temperature T_e , and principal quantum number n is (Brocklehurst and Seaton 1972):

$$\frac{\Delta v_T}{\Delta v_{\text{th}}} = \left\{ 1 + \left[0.17 \left(\frac{n}{100} \right)^{7.4} \left(\frac{N_e}{10^4} \right) \left(\frac{10^4 \text{ K}}{T_e} \right)^{0.1} \right]^2 \right\}^{1/2}. \quad (3)$$

For $N_e = 10^5$ and $T_e = 10,000 \text{ K}$, we find $\Delta v_T/\Delta v_{\text{th}} = 1.03$ and 1.003 for $n = 76$ and 66 , respectively. Thus, pressure broadening is negligible for both lines.

The electron density, emission measure, Lyman continuum flux, and the mass of ionized gas have been derived following the formulation of Schraml and Mezger (1969) for spherically symmetric Gaussian sources, using the formulas given by Rodriguez *et al.* (1980). For nonspherical sources, we used the geometric mean of the largest and smallest angular diameters at half-maximum as the equivalent angular diameter at half-maximum in the spherical source. In Table 5 we list the observing frequency, electron temperature, the electron density, the emission measure, the number of ionizing photons, the continuum optical depth, and the approximate spectral type of the exciting star for each of the observed H II regions.

TABLE 2
OBSERVATIONAL PARAMETERS OF COMPACT H II REGIONS

SOURCE ^a	COORDINATES (1950)		FLUX DENSITY (Jy)	DECONVOLVED SIZE (")	COMMENT ^b
	Right Ascension	Declination			
14.7 GHz					
W3(OH)	02 ^h 23 ^m 16 ^s .43	61°38'57".3	2.0 ^c	1.4 × 1.5 ^c	OH
Sgr B2:					
North (MD4)	17 44 10.69	-28 21 12.0	6.6	11.8 × 11.9	
Main ^d (MD5)	10.66	22 03.5	10.9	8.2 × 7.9	OH
South	10.65	22 42.3	0.9	3.7 × 0.6	OH
W49S:					
K	19 07 58.16	09 00 05.2	4.1	4.9 × 2.2	OH
L	58.54	07.6	3.0	10.7 × 6.6	
W51:					
d	19 21 22.25	14 25 15.6	10.3	6.3 × 5.5	
e	24.28	24 43.1	10.7	13.5 × 6.9	
e1	26.22	24 41.0	0.26	1.9 × 1.5	OH
22.4 GHz					
W3(OH)	02 ^h 23 ^m 16 ^s .49	61°38'57".3	2.1	1.4 × 1.4	OH
G10.6-0.4 A + B	18 07 30.67	-19 56 29.0	3.8	3.5 × 2.5	OH
G19.6-0.2:					
A	18 24 50.31	-11 58 34.5	0.78	3.6 × 2.1	
B	49.51	27.1	0.15	1.6 × 0.6	
C1	50.21	30.4	0.16	2.0 × 0.8	OH
C2	50.24	27.2	0.33	4.0 × 2.2	
D	50.49	23.5	0.18	2.3 × 1.5	
G20.1-0.1:					
A	18 25 23.19	-11 30 46.0	0.41	2.1 × 1.9	
B	23.05	44.9	0.37	0.6 × 0.3	OH
G34.3+0.2	18 50 46.14	01 11 12.5	5.2	2.1 × 1.5	OH
G45.1+0.1	19 11 00.41	10 45 42.9	0.9	0.8 × 0.6	OH

^a Capital letters correspond to the notation of Ho and Haschick 1981 for G10.6-0.4, G19.6-0.2, and G20.1-0.1 and to the notation of Wink, Altenhoff, and Webster 1975 for W49S. MD numbers in Sgr B2 correspond to components given in Martin and Downes 1972.

^b OH: OH maser emission most closely associated with this component.

^c Data from Dreher and Welch 1981.

^d Triple source.

TABLE 3
LINE PARAMETERS^a

Source	Transition	Velocity ^b (km s ⁻¹)	Line Width ^c (km s ⁻¹)	T_L/T_c^d
W3(OH)	H76 α	-51.2 ± 0.2	42.1 ± 0.6	0.068 ± 0.001
Sgr B2M	H76 α	60.3 ± 0.5	34.3 ± 1.4	0.089 ± 0.003
Sgr B2S	H76 α	54.5 ± 0.5	37.2 ± 1.4	0.102 ± 0.003
W49S	H76 α	7.2 ± 0.4	39.9 ± 1.2	0.120 ± 0.003
W51e	H76 α	58.3 ± 0.6	25.4 ± 1.5	0.204 ± 0.009
W51d	H76 α	60.5 ± 0.3	27.0 ± 0.7	0.183 ± 0.004
W3(OH)	H66 α	-49.6 ± 0.2	38.3 ± 0.6	0.165 ± 0.002
G10.6-0.4	H66 α	-1.2 ± 0.2	33.3 ± 0.8	0.211 ± 0.003
G19.6-0.2	H66 α	35.3 ± 0.5	29.5 ± 1.3	0.341 ± 0.011
G20.1-0.1	H66 α	42.7 ± 0.6	29.1 ± 1.7	0.200 ± 0.009
G34.3+0.2	H66 α	45.8 ± 0.6	54.7 ± 2.5	0.116 ± 0.004
G45.07+0.13	H66 α	47.7 ± 0.7	42.3 ± 2.3	0.158 ± 0.006

^a Errors are formal 1 σ values for the model of a Gaussian line shape plus linear baseline model.

^b With respect to the local standard of rest.

^c Full width at half-maximum.

^d Ratio of the flux density of the line to the flux density of the continuum.

TABLE 4
OH MASERS

SOURCE	V (LSR) (km s ⁻¹)	COORDINATES (1950)		POLARIZATION	FLUX DENSITY (Jy)	
		Right Ascension	Declination			
Sgr B2	73.1	17 ^h 44 ^m 10 ^s .614	-28°22'43".63	L	7.3	
	71.5	10.619	43.52	L	21.6	
	69.8	10.638	43.01	L	39.1	
	67.7	10.647	42.78	L	205.	
	64.3	10.318	03.14	L	2.5	
	62.3	10.341	02.75	L	23.3	
	59.9	10.336	02.55	L	6.4	
G10.6-0.4	3.4	18 07 30.577	-19 56 28.07	R	0.4	
	0.4	30.615	28.84	R	1.0	
	-2.2	30.605	28.98	R	18.8	
	2.9	30.735	29.00	L	0.3	
	2.3	30.622	28.58	L	0.3	
	0.1	30.607	28.80	L	4.9	
	-2.1	30.607	28.87	L	5.1	
G19.6-0.2	43.1	18 24 50.245	-11 58 30.75	R	1.5	
	42.0	50.241	30.70	R	8.9	
	40.9	50.238	30.66	R	3.9	
	38.7	50.224	30.82	R	0.2	
	44.2	50.243	30.76	L	0.8	
	43.1	50.244	30.74	L	1.1	
	42.0	50.238	30.73	L	1.2	
	40.9	50.237	30.68	L	0.4	
	40.9	50.190	31.13	L	0.5	
	39.8	50.224	30.92	L	0.2	
	37.6	50.219	31.76	L	0.2	
	49.7	18 25 23.013	-11 30 44.11	R	2.1	
G20.1-0.1	48.6	23.024	44.16	R	2.6	
	47.5	23.030	44.24	R	0.6	
	45.3	23.033	44.19	R	0.8	
	43.1	23.032	44.23	R	1.1	
	42.0	23.038	44.18	R	0.4	
	48.6	23.021	44.28	L	0.4	
	46.3	23.015	44.09	L	8.5	
	44.2	23.021	44.18	L	0.9	
	43.1	23.030	44.27	L	0.7	
	42.0	23.031	44.44	L	0.4	
	G34.3+0.2	59.3	18 50 46.275	01 11 14.34	R	13.1
		58.2	46.242	12.40	R	36.4
55.5		46.210	11.50	R	1.4	
60.8		46.242	12.46	L	1.8	
59.2		46.261	14.51	L	2.5	
58.2		46.241	12.44	L	8.0	
56.0		46.279	14.33	L	11.9	
W49S	20.1	19 07 58.010	09 00 04.51	R	10.7	
	16.3	58.044	04.92	R	118.	
	13.5	58.065	03.39	R	67.7	
	19.0	58.051	04.57	L	48.0	
	17.4	58.022	04.62	L	90.0	
	15.7	58.040	04.87	L	51.0	
	13.5	58.066	03.41	L	52.5	
G45.07+0.13	61.5	19 11 00.409	10 45 44.92	R	5.1	
	60.5	00.407	43.44	R	7.4	
	56.6	00.423	43.62	R	30.5	
	53.8	00.414	43.60	R	4.3	
	61.5	00.368	43.38	L	3.0	
	61.5	00.391	44.91	L	0.6	
	58.2	00.480	42.94	L	0.3	
	53.9	00.414	43.61	L	16.0	
W51	61.7	19 21 26.307	14 24 35.07	R	12.2	
	59.6	26.263	40.83	R	20.9	
	59.3	26.305	35.15	R	105.	
	58.4	26.261	40.74	R	12.8	
	57.3	26.256	40.62	R	4.9	
	56.2	26.258	36.50	R	0.7	
	56.2	26.252	40.53	R	1.4	
	61.7/58.4	26.306	35.12	L	121.	
	57.3	26.312	35.20	L	4.3	
	57.2	26.278	33.24	L	2.6	
	57.3	26.250	40.75	L	0.7	
	56.2	26.267	40.84	L	0.5	
	54.7	26.266	40.73	L	0.6	
	50.2	26.254	40.72	L	0.4	
47.7	26.318	40.90	L	1.0		

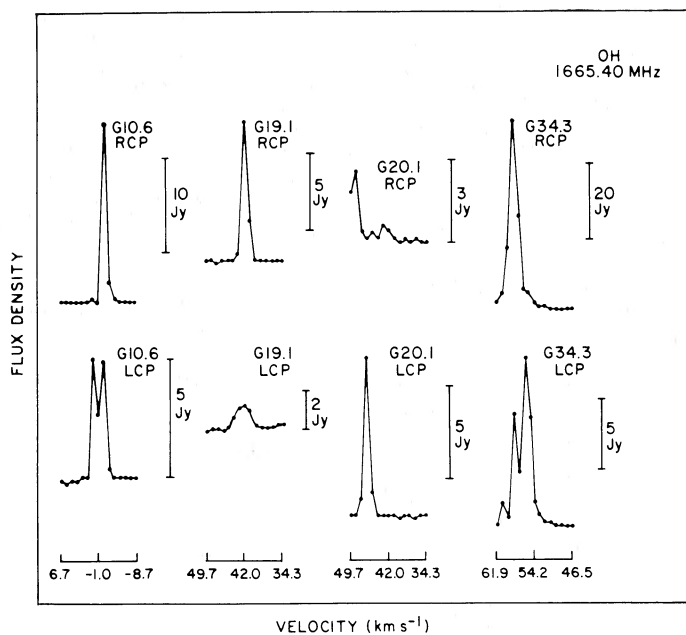


FIG. 10a

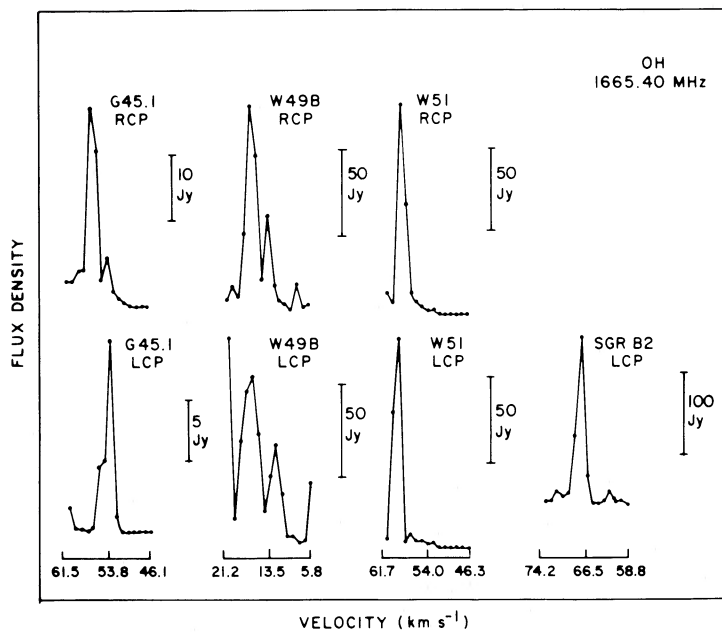


FIG. 10b

FIG. 10.—OH spectra at 1665.40 MHz summed over each source. The velocity axis is referred to the local standard of rest. The upper and lower panels correspond to the right and left circular polarization observations, respectively.

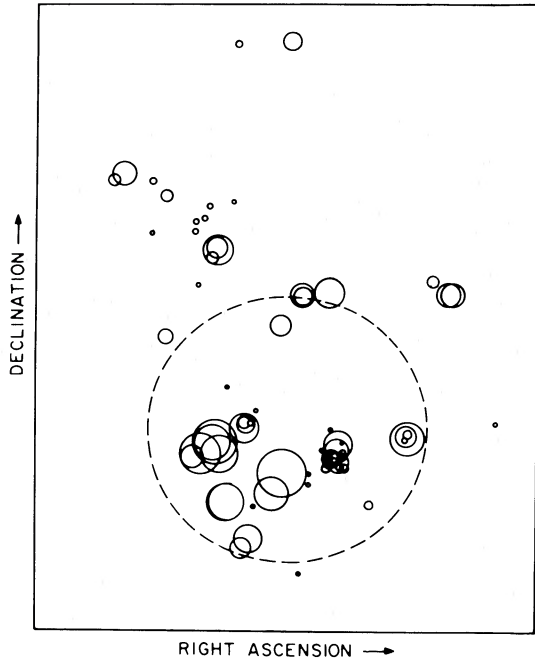


FIG. 11.—Schematic map of all the OH maser spots in the right and left circular polarization projected against their associated compact H II region. The deconvolved size of the H II regions is shown as the dashed circle. The positions of the masers are measured with respect to the center of the associated compact H II region in units of the radius of the compact H II region.

b) OH Maser Emission

Table 6 gives the velocity characteristics of the OH masers associated with compact H II regions. Column 2 gives the average velocity of all OH features in the right and left circular polarization maps. Columns 3 and 4 give the midpoint of the velocity extremes and the velocity range of the OH emission, respectively. In some cases the maser components show alignments and systematic gradients in velocity, similar to the one observed in W75N (Haschick *et al.* 1981). However, when maps with both senses of circular polarization are combined, the systematic motions are less clear.

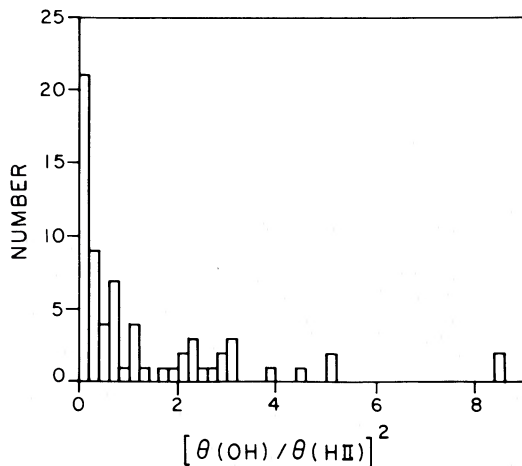


FIG. 12

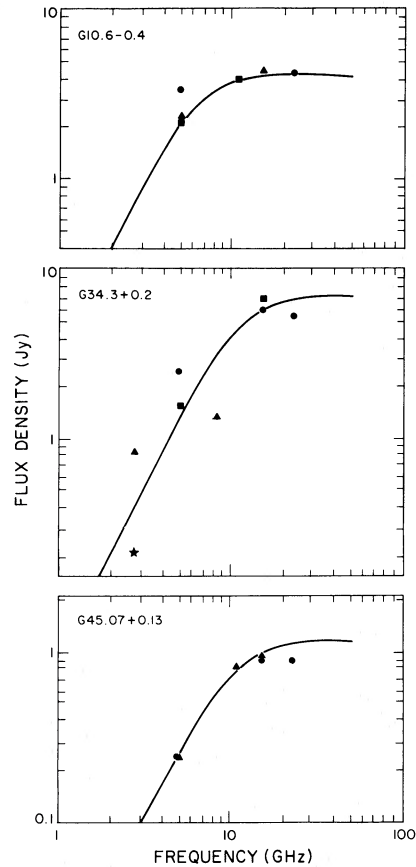


FIG. 13

FIG. 12.—Distribution of OH maser spots shown in Fig. 11 as a function of the relative radial distance from the center of the associated compact H II region in equal area steps.

FIG. 13.—Microwave spectrum of some of the compact H II regions with associated OH maser emission.

About 25% of the OH maser spots in our sample show emission in both right and left circular polarization. In Table 7 we list the characteristics of the OH features identified in right and left circular polarization that emanate from within $0''.05$ of each other. The difference in velocity between these right and left circularly polarized spots is most simply explained by the Zeeman effect (Goldreich, Keeley, and Kwan 1973). In the presence of a magnetic field, the upper and lower levels of the (${}^2\pi_{3/2}$, $J = 3/2$, $F = 1-1$)-transition are each split into three sublevels giving rise to a pair of oppositely elliptically polarized lines (σ components) straddling a linearly polarized line (π component). For a magnetic field of strength B , the velocity separation between the σ components is (e.g., Davies 1974),

$$\Delta v = \frac{2c}{v} \frac{g\mu B}{h}, \quad (4)$$

where $\mu = 9.27 \times 10^{-21}$ ergs gauss $^{-1}$ (the Bohr magneton), h is Planck's constant, and g is the Landé factor of the lower state of the transition. For the (${}^2\pi_{3/2}$, $J = 3/2$, $F = 1-1$)-OH-transition at 1665.4 MHz, $g = 1.17$, and the velocity separation of σ components, Δv , is given by $\Delta v = 0.59 B$, where B is in milligauss and Δv in km s $^{-1}$. In the last column of Table 7 we give the strength of the magnetic field necessary to shift the velocities of the σ components by the observed amount. The typical magnetic field strengths are about 6 milligauss. Similar

TABLE 5
DERIVED PARAMETERS FOR THE OBSERVED H II REGIONS

Source (1)	ν (GHz) (2)	T_e^* (K) (3)	N_e (10^4 cm^{-3}) (4)	EM (10^8 pc cm^{-6}) (5)	N_l (10^{49} s^{-1}) (6)	τ (7)	Spectral Type (8)
W3OH	22	8000	13.	5.0	0.16	0.31	O8.5
Sgr B2 Main	15	10000	1.2	0.84	11.	0.09	O4
Sgr B2 South	15	8400	4.1	1.8	0.82	0.25	O6.5
G10.6-0.4	22	7300	3.9	1.9	1.3	0.13	O6
G19.6-0.2	22	5400	2.4	0.44	0.11	0.05	O9
G20.1-0.1 (A)	22	8600	2.9	0.49	0.06	0.03	O9.5
G34.3+0.2	22	8000	10.	5.3	0.56	0.33	O6.5
W49S (K)	15	6800	2.2	1.6	7.2	0.31	O4
G45.07+0.13	22	7100	12.	6.7	0.64	0.50	O6.5
W51d	15	6600	2.0	1.2	4.8	0.24	O5
W51e	15	6400	1.0	0.47	4.9	0.10	O5

NOTES: (1) source name; (2) frequency of data from which parameters were derived; (3) electron temperature from LTE analysis (eq. 1); (4) electron density; (5) emission measure; (6) Lyman continuum photon rate; (7) opacity at frequency ν given in column (2); (8) spectral type from models of Panagia 1973.

TABLE 6
OH VELOCITIES

Source (1)	$\langle v \rangle$ (km s^{-1}) (2)	v_m (km s^{-1}) (3)	Δv (km s^{-1}) (4)
W3(OH) ^a	-44.6	-44.6	7.8
Sgr B2 S ^b	70.5	70.4	5.4
Sgr B2 M ^b	62.2	62.1	4.4
G10.6-0.4	0.7	0.5	5.3
G19.6-0.2	41.2	40.9	5.5
G20.1-0.1	45.5	45.6	7.2
G34.3+0.2	58.2	57.9	4.3
W49S	16.5	16.5	6.1
G45.07+0.13	58.4	57.7	7.7
W51e1	55.3	55.2	6.5
W51e2	58.6	59.2	5.0

NOTES: (1) source name; (2) average velocity of maser features; (3) midpoint of velocity range of maser emission; (4) velocity range of maser emission.

^a Data from Reid *et al.* 1980.

^b LCP feature only.

values have been deduced from interferometric studies of masers (e.g., Lo *et al.* 1975; Moran *et al.* 1978; Reid *et al.* 1980; and Norris and Booth 1981).

Some of the features in Table 7 appear at the same velocity in the right and left circular maps, as expected for π components. However, the flux densities in the two polarizations are generally different. Therefore, those features cannot be identified with the linearly polarized π components. They are either isolated σ components with elliptical polarization or blended σ and π components in regions of small magnetic field.

V. COMMENTS ON INDIVIDUAL SOURCES

Compact H II regions are usually found in groups and often are projected toward a lower-density medium (Habing and Israel 1979). Therefore, aperture synthesis observations with angular resolution similar to the angular sizes of the compact H II regions are necessary to study their properties. In particular, single-antenna observations and aperture synthesis observations are not easily compared since the emission seen by a single antenna can be dominated by an extended region while a

TABLE 7
POSSIBLE ZEEMAN PAIRS

SOURCE (1)	V (LSR)		FLUX DENSITY				B (mGauss) (6)
	R (km^{-1}) (2)	L (km^{-1}) (2)	R (Jy) (3)	L (Jy) (3)	d ($''$) (4)	v (km s^{-1}) (5)	
G19.6-0.2	43.1	43.1	1.5	1.1	0.02	0.0	...
	42.0	42.0	8.9	1.2	0.05	0.0	...
	40.9	40.9	3.9	0.4	0.02	0.0	...
G20.1-0.1	49.7	46.3	2.1	8.5	0.04	3.4	6
	48.6	44.2	2.6	0.9	0.05	4.4	7
	47.5	43.1	0.6	0.7	0.03	4.4	7
G34.3+0.2	43.1	...	1.1	...	0.05	0.0	...
	59.3	56.0	13.1	11.9	0.06	3.3	6
	58.2	58.2	36.4	8.0	0.04	0.0	...
W49S	...	60.8	...	1.8	0.06	-2.6	-4
	13.5	13.5	67.7	52.5	0.02	0.0	...
	53.8	53.9	2.8	10.8	0.01	-0.1	...
G45.07+0.13	59.6	56.2	20.9	0.5	0.06	3.4	6
	58.4	54.7	12.8	0.6	0.07	3.7	6

NOTES: (1) source name; (2) velocities of possible Zeeman pairs; (3) flux densities; (4) angular separation between R and L circular features; (5) velocity separation; (6) magnetic field positive toward observer. See text (§ IVb) for discussion of cases where there is no velocity separation of features.

synthesis instrument detects only the radiation from compact components. Comparison with previous observations will be made only in the cases in which similar beamwidths were used.

a) W3(OH)

W3(OH) is an H II region near the Cas OB6 association at a distance of about 2.2 kpc from the Sun (Humphreys 1978). OH maser maps at 1665 MHz by Reid *et al.* (1980) and at 6035 MHz by Moran *et al.* (1978) show that most of the maser spots are projected against the compact H II region.

Results of radio continuum measurements of the free-free emission from W3(OH) have been compiled by Hughes and Viner (1976). From these data they derived a turnover frequency of 11.8 GHz, which implies an emission measure of about $5 \times 10^8 \text{ pc cm}^{-6}$. Table 8 gives information about recent recombination-line measurements. Single antenna and aperture synthesis results are in good agreement, suggesting that any diffused emission around W3(OH) is very weak. Interferometric maps at 22 GHz by Dreher and Welch (1981) and at 30 GHz by Scott (1981) suggest that the ionized gas is in a shell. Both papers argue that the ionized shell is the inner edge of a cocoon of dust and gas which is being pushed outward by the radiation pressure from a young, embedded luminous star.

b) Sagittarius B2

Sgr B2, located within a few hundred parsec of the galactic center, is one of the most spectacular molecular clouds of our Galaxy. It is the site of complex interstellar molecules, masers, and newly formed early-type stars. Previous interferometric observations at 5 GHz by Martin and Downes (1972, hereafter MD) and Downes *et al.* (1979) show that the 2' central region of Sgr B2 consists of four compact H II regions (MD components 3, 4, 5, and 6). Our map shows that source MD5 has considerable structure. There are at least two distinct components (see Fig. 2). More components may be present, but a higher angular resolution map (of $\sim 1''$) is needed to separate them. Within the 2' central region, we also detected a compact H II region about $40''$ south of the MD5 component. This source was also detected by Benson and Johnson (1984).

Our VLA map of the OH emission shows that it originates from two centers of emission separated by $40''$ in the north-south direction. The southern region OH emission is the strongest and is coincident in angle with the newly detected compact H II region. The northern OH region is associated with the most compact component in the source MD5.

The H₂O maser emission from Sgr B2 originates in three regions equally spaced by $\sim 44''$ along the north-south direction and with sizes of $2''$ or less (Elmegreen *et al.* 1980). The

middle and southern H₂O sources fall close to the compact H II regions associated with the OH emission.

c) G10.6-0.4

The distance to G10.6-0.4 is poorly known because of the kinematic distance ambiguity and the lack of optical observations. For the derivation of physical parameters, we used the near kinematic distance of 6 kpc adopted by Downes *et al.* (1980) from a study of the H₂CO absorption line at 4.8 GHz. Previous high-resolution ($\sim 0''.3$) radio observations toward this source were made by Ho and Haschick (1981). Their 15-GHz continuum map shows that the source consists of two compact H II regions of angular sizes of $2''.8$, separated by $1''.5$, having an integrated flux density of 4.2 Jy. Our observed flux density of 3.8 Jy at 22 GHz (corresponding to the flux density of both components) is close to the value of Ho and Haschick at 15 GHz. This suggests that both compact components are thin at both frequencies.

d) G19.6-0.2

The G19.6-0.2 complex has a distance of 4 kpc (Matthews *et al.* 1977) and is one of the best examples of the clumpy nature of some compact H II regions. Ho and Haschick (1981) mapped the region at 5 GHz with an angular resolution of $1''$ and found five compact H II regions within an angular diameter of $\sim 30''$ ($\sim \frac{1}{2}$ pc at 4 kpc). Our map at 22 GHz agrees well with the map of Ho and Haschick at 5 GHz. The flux density at 5 and 22 GHz of the strongest member of the complex (component A) agrees well with the values expected for an H II region that is thin at frequencies greater than 5 GHz. One important difference between these two maps is the detection at 22 GHz of a new ultracompact source which is not seen at 5 GHz. Our map of the OH emission toward the complex shows that the OH maser spots are projected on the face of the newly detected, ultracompact H II region (see Fig. 4).

e) G20.1-0.1

The near kinematic distance for G20.1-0.1 is 4 kpc (Matthews *et al.* 1977; Downes *et al.* 1980). This source was mapped at 5 GHz by Ho and Haschick (1981), and consists of two compact components separated by $\sim 2''$ and a third component $\sim 40''$ to the south. Our measurements of the flux densities at 22 GHz are 1.3 and 2.1 times higher than those at 5 GHz made by Ho and Haschick. This result suggests that these H II regions become optically thin at about 8 GHz. Our map of the OH maser spots shows that the OH emission is associated with the strongest and most compact component at 22 GHz.

f) G34.3+0.2

This complex H II region G34.3+0.2 is located $\sim 40'$ from the supernova remnant W44 at a distance of 3.8 kpc. Interferometric continuum observations at 2.7 GHz show that it consists of four components spread over $\sim 60''$ (Turner *et al.* 1974). In Figure 14 we present VLA maps of this region at 5, 15, and 22 GHz. The OH maser emission is associated with the most compact H II component. The OH maser spots (see Fig. 6) are approximately aligned in a direction perpendicular to the line through the core of the two compact components. The alignment suggests a disk geometry for the OH maser emission. However, the velocity structure of the maser features do not show the organized motions expected for a rotating disk. The recombination-line velocity of the ultracompact component associated with the OH emission is 45.8 km s^{-1} , about 7 km

TABLE 8
W3(OH) RECOMBINATION LINE PARAMETERS

Line	Center Velocity (km s ⁻¹)	Line Width (km s ⁻¹)	Line-to-Continuum Ratio	Ref.
H66 α	-50.1 \pm 1.1	33 \pm 3	0.18 \pm 0.03	(1)
H66 α	-48.9 \pm 0.4	37.8 \pm 1.2	0.13 \pm 0.02	(2)
H66 α	-49.6 \pm 0.2	38.3 \pm 0.6	0.165 \pm 0.003	(3)
H76 α	-51.3 \pm 1.0	42.4 \pm 2.7	0.063 \pm 0.005	(2)
H76 α	-51.2 \pm 0.2	42.1 \pm 0.6	0.068 \pm 0.001	(3)

REFERENCES: (1) Jaffe, Wilson, and Thomasson 1978. (2) Thum, Mezger, and Pankonin 1980. (3) This paper.

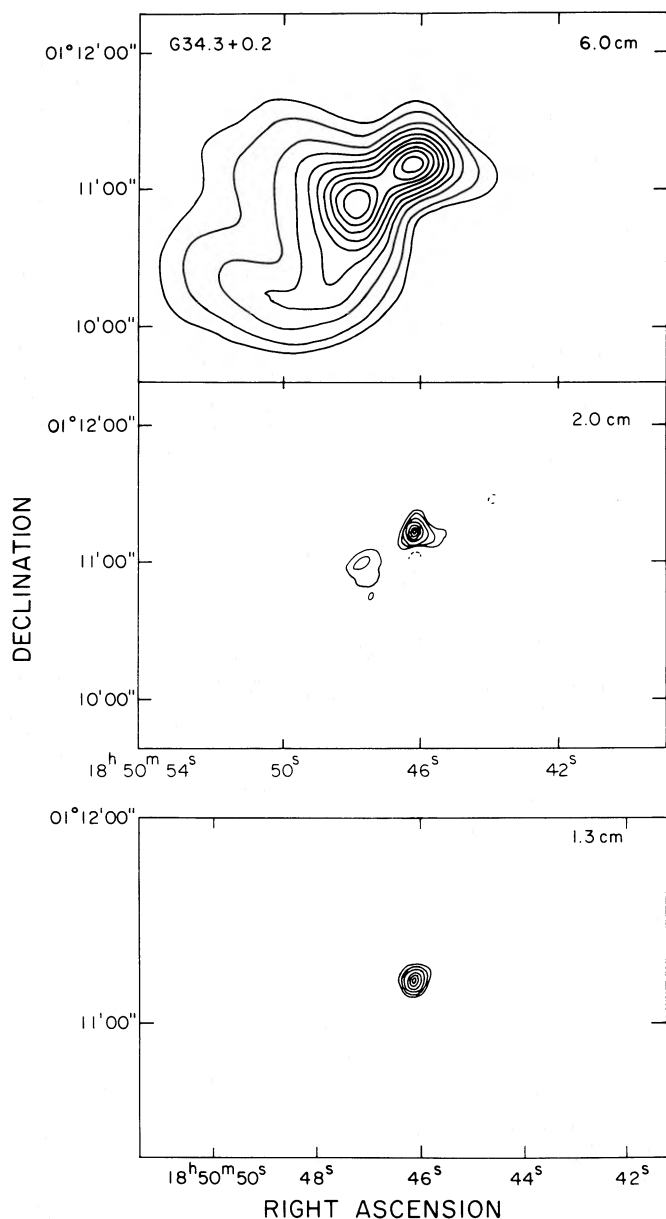


FIG. 14.—VLA continuum snapshots of the star-forming region G34.3+0.2 at 5.0 GHz (6 cm), 14.7 GHz (2 cm), and 22.4 GHz (1.3 cm), respectively.

s^{-1} less than the recombination-line velocity of 53.0 km s^{-1} derived with single-antenna observations for the more extended components (Downes *et al.* 1980).

g) W49S

W49S is the easternmost of six components embedded in the giant ($\sim 30 \text{ pc}$) H II region W49A (Wynn-Williams 1971). Our VLA continuum map of W49S at 14.7 GHz (see Fig. 7) can be modeled by two components with angular sizes of 8.4 and 3.3, respectively, and an angular separation of $\sim 6''$. This is in good agreement with the model of the radio emission at 8.1 GHz by Wink, Altenhoff, and Webster (1975). The flux density of the most compact component (component K) at 8.1 and 14.7 GHz suggests that it has a turnover frequency of $\sim 10 \text{ GHz}$.

Intense hydroxyl and water maser emission has been found toward the region. Rogers *et al.* (1967) and Raimond and

Eliasson (1969) showed that main-line OH emission comes from W49S and from W49N, two of the compact H II regions in the giant complex. Hardebeck (1971) found that the 1720 MHz satellite-line emission arises only from W49S. The H_2O emission toward W49N spans a large velocity range of $\sim 500 \text{ km s}^{-1}$. VLBI observations show that the H_2O emission arises from over 300 features in several groups toward W49N (Walker, Matsakis, and Garcia-Barreto, 1982). Our VLA map of the OH maser emission toward W49S shows that it is associated with the most dense and compact H II component. The water maser in W49S is also associated with this component (Genzel and Downes 1977).

Previous interferometric recombination-line observations toward W49S were made by van Gorkom *et al.* (1980) in the H109 α line. However, because of the insufficient angular resolution and the low observing frequency, their measurement corresponds to an average value between components K and L, probably significantly weighted by the less compact components.

h) G45.07+0.13

G45.07+0.13 is located in a group of extended H II regions near $l = 45^\circ$, $b = 0^\circ$ at a kinematic distance of 9.7 kpc (Matthews *et al.* 1977). The region was mapped interferometrically at 5 GHz with the WSRT by Matthews *et al.* (1977), who found an unresolved source (angular size $< 5''$) with a flux density of 0.25 Jy. Our VLA synthesis map toward this region at 22 GHz shows that it consists of a single compact H II region having an angular size of $\sim 0.7''$.

Figure 12 shows the spectrum of this source, derived from VLA snapshot observations at 5, 15, and 22 GHz. Also plotted are the continuum flux densities at 10.7 and 15 GHz measured with the 100-m Bonn telescope by Matthews *et al.* (1977). The good agreement between the flux densities measured with single-antenna and synthesis instruments suggests that there is little extended emission. The observed spectrum of this source is well modeled by the theoretical spectrum of a spherical H II region with a radius of 0.04 pc, electron density of $8 \times 10^4 \text{ cm}^{-3}$, electron temperature of 7100 K, and located at a distance of 9.7 kpc.

i) W51A

W51A is a giant H II region located at a distance of 7 kpc (Genzel *et al.* 1981, 1982; Schneps *et al.* 1981). At 2.7 GHz, W51A consists of eight compact components spread over a radius of $\sim 6''$, and which are embedded in a diffuse, ionized envelope (Martin 1972). Our observations at 14.7 GHz were toward the compact component W51e, believed to be associated with the OH maser emission (see Fig. 9). The field of view also included the compact component W51d.

The flux density at 14.7 GHz of the W51d region measured with the VLA is consistent with the 5 GHz flux measured with the Cambridge One-Mile interferometer (Martin 1972), assuming that the H II region is thin at both frequencies. Thus most of the radio emission arises in a region of angular size of $\sim 6''$ as measured with the VLA. On the other hand, the flux density at 15 GHz of W51e measured with the VLA is $\sim 60\%$ less than observed at 5 GHz with the Cambridge One-Mile interferometer (Martin 1972), implying that most of the radio emission arises in an extended region highly resolved by the VLA. A weak ($\sim 200 \text{ mJy}$), ultracompact component has been detected east of W51e, which we designate W51e1.

Our VLA map of the OH maser spots shows that the OH

maser emission arises from two small regions separated by $\sim 5''$ eastward of the H II region W51e. Both OH sources are closely associated with strong water maser centers of activity (Genzel *et al.* 1981). The strong OH emission center is associated with W51MAIN, the strongest H₂O maser source in the area. W51MAIN consists of intense, low-velocity H₂O features ($V_{\text{LSR}} = 50\text{--}70 \text{ km s}^{-1}$) concentrated toward the center of the source and weak, high-velocity ($V_{\text{LSR}} = 70\text{--}160 \text{ km s}^{-1}$) masers located in a shell surrounding the core of low-velocity lines (Genzel *et al.* 1981). Projection of the OH maser spots on our 15-GHz radio continuum map of W51 shows that the strongest OH center of activity is coincident with the position of the ultracompact H II region W51e1. In addition, Ho, Genzel, and Das (1983) have found that the OH/H₂O sources are also coincident with warm ($\sim 100 \text{ K}$) NH₃ condensations.

VI. DISCUSSION

a) OH Masers/Compact H II Region Association

Our maps show that OH masers often occur in multiple-component H II region complexes and are associated with the most dense and compact H II component in the complex. The OH maser spots are, in most of the cases, projected within the half-power diameter of the compact H II region as measured at 15 or 22 GHz (see Figs. 11 and 12 and the discussion in § IIIc). Furthermore, the probability of finding an OH maser spot is highest toward the center of the compact H II region. Were the brightest OH masers to lie in a ring near the limb of the compact H II region (e.g., Cook 1968; Baldwin, Harris, and Ryle 1973; Elitzur and de Jong 1978; Ho and Haschick 1981), then the histogram in Figure 12 would have shown a peak near $\Theta(\text{OH})/\Theta(\text{H II}) = 1$. Instead we find a peak near the origin. This does not support the model in which the OH masers are observed preferentially toward the limbs of the H II regions as suggested by Ho *et al.* (1983). Instead, the preference of the OH spots to project onto the face of a compact H II region supports the theory that OH masers are amplifying radiation from the background H II region (Reid *et al.* 1980). Note, however, that the analysis of the data in Figures 11 and 12 is prone to errors because of inadequate resolution of multiple components of the continuum emission and inadequate sensitivity to weak sources. Just as we have detected more structure than previously reported for some of the regions, more sensitive observations in the future are likely to detect additional structure.

b) Dynamics of the Masing Region

To investigate the dynamical relationship between the OH maser sources and the underlying star, we need to know the velocity of the star and the mean velocity of the OH maser condensations. We assume that the velocity of the star is given by the centroid of a hydrogen recombination line from the compact H II region which surrounds the star. The hydrogen recombination lines we observed are optically thin, but they are formed in a region whose continuum optical depth can be significant. If the line excitation temperature and electron temperature are equal then there would be no bias in the line velocity due to the complex transfer of radiation through a compact H II region. However, to minimize possible shifts in the centroid of a recombination line which might occur under non-LTE conditions, it is best to observe a transition frequency high enough so that the continuum opacity is low. For most of our sources $\tau < 0.5$; hence, we expect our recombination line centroids to be a fairly accurate indicator of the central star's radial velocity. However, in some cases radiative transfer effects could make the recombination-line velocity slightly blueshifted with respect to the stellar velocity.

The OH maser spots typically exhibit a radial velocity spread of about 5 km s^{-1} . This is due in part to Zeeman splitting (4 km s^{-1} for 6 milligauss) and in part to internal dynamics. The mean radial velocity of the OH maser spots was taken as the average velocity of the OH features in the right and left circular polarization maps, which should minimize errors introduced by Zeeman splitting. The good agreement between this velocity estimate and the midpoint velocity (columns 2 and 3 in Table 6) gives further support to the reliability of the estimate of the mean velocity of the maser emission.

In Table 9, we compile the velocities of the compact H II regions, the mean radial velocities of the OH maser spots, and the differences between the H II and OH velocities. For our sample, the mean radial velocity of the OH masers always is greater than (redshifted from) the velocity of the associated compact H II region. Since the turnover frequencies of the ultracompact H II regions are about 10 GHz, we estimate that their optical depth at the OH emission frequency of 1.6 GHz are about 70. Thus, OH masers projected against compact H II regions must come from the near side of the region. Thus, the OH masers appear to be moving toward the underlying star.

TABLE 9
OH MASERS/COMPACT H II REGION VELOCITIES

SOURCE	LINE	VELOCITIES (km s^{-1})			MASS M_{\odot}
		Compact H II ^a	OH ^b	OH-Compact H II	
W3(OH)	H76 α	-51.2	-44.6 ^c	6.6	110
	H66 α	-49.6	-44.6 ^c	5.0	...
Sgr B2 M	H76 α	60.3	62.2	1.9	160
Sgr B2 S	H76 α	54.5	70.5	16.0	2300
G10.6-0.4	H66 α	-1.2	0.7	1.9	36
G19.6-0.2	H66 α	35.3	41.2	5.9	100
G20.1-0.1	H66 α	42.7	45.5	2.8	18
G34.3+0.2	H66 α	45.8	58.2	12.4	800
W49S	H76 α	7.2	16.5	9.3	2200
G45.07+0.13	H66 α	47.7	58.4	10.7	430
W51e	H76 α	58.3

^a Compact H II region velocities derived in this paper.

^b Mean radial velocity calculated as described in the text.

^c Average velocity from Reid *et al.* 1980.

This result strongly constrains models for the dynamics of the masing region.

The model proposed by Cook (1968) and developed by Elitzur and de Jong (1978), in which the OH maser spots are confined to an expanding shell between the shock and the ionization fronts which bounds the compact H II region, fails to explain the observed relative velocities. Were the maser emission to arise from a thin shell formed after the passage of a shock expanding from the star, material on the near side of the shell would have a lower velocity (blueshifted) with respect to the star.

Our observations support the model, developed by Reid *et al.* (1980), that OH masers are formed in collapsing envelopes of remnant material surrounding very young stars. However, in some cases, the velocity differences between the OH masers and the H II region recombination lines are considerably larger than would be expected for gravitational free fall. Table 9 lists the central mass required for free fall at the observed radius of the H II region. Some of the mass estimates exceed 100 solar masses and are probably too large for single O stars or small stellar groups. This may indicate that, in some cases, a part of the velocity shift between the OH masers and the hydrogen recombination line is not due to gravitational collapse. We reiterate that some of our estimates of stellar velocities could be in error for two reasons: radiative transfer effects in the recombination lines and inadequate angular resolution to resolve structure in the H II regions.

While the observational results for gravitational collapse are not yet conclusive, there is a substantial theoretical basis for such a model. Calculations of the evolution of a massive ($> 10 M_{\odot}$), collapsing protostar (Larson 1973) shows that a dense inner core forms in the earlier stages of gravitational contraction and has a time scale for radiative cooling and contraction shorter than the time scale for infall of the remaining protostellar material. Thus, the core evolves rapidly to the main sequence while still surrounded by its remnant accreting protostellar envelope. After attaining a sufficiently high mass and luminosity, the core may interact with the infalling material, tending to inhibit the further collapse of the surrounding cloud (Larson and Starrfield 1971).

c) Evolutionary Stages

The OH masers seem to be formed in a collapsing envelope of neutral material which encompass an ionized, dense and compact remnant of the prestellar cloud surrounding a newly formed O or B star. The ionization front ultimately might expand through the neutral material and dissociate the OH molecules. This may be the reason that the extended H II regions within a complex, such as W51N and W51MAIN in the W51A region, do not show OH maser emission (Habing *et al.* 1974).

d) Physical Conditions of Compact H II Regions

In the absence of pressure broadening and non-LTE effects, the observed line width of a recombination line is determined by thermal, Δv_{th} , and turbulent, Δv_{turb} , motions and is given by

$$\Delta v = (\Delta v_{\text{th}}^2 + \Delta v_{\text{turb}}^2)^{1/2}. \quad (5)$$

Table 10 gives the observed line widths, the thermal line widths, and the turbulent line widths for the observed compact H II regions. The average of the full-widths at half-intensity for these compact H II regions is $\sim 35 \text{ km s}^{-1}$, about 5 km s^{-1} broader than that of typical high-density H II regions (Lichten,

TABLE 10
LINE WIDTHS FROM HIGH-DENSITY COMPACT H II REGIONS

SOURCE	WIDTH (km s^{-1}) ^a		
	Observed	Thermal	Turbulent
Sgr B2 M	34.3	21.5	16.1
Sgr B2 S	37.2	19.6	19.0
G10.6-0.4	33.3	18.3	16.7
G19.6-0.2	29.5	15.6	15.0
G20.1-0.1	29.1	19.9	12.8
G34.3+0.3	54.7	19.1	30.8
W49S	39.9	17.7	21.5
G45.07+0.13	42.3	18.7	22.8
W51e	25.4	17.1	11.3
W51d	27.0	17.4	12.4
W3(OH)	42.1	22.1	21.5
	38.3	19.2	19.9

^a Full width at half-intensity.

Rodriguez, and Chaisson 1979) and 10 km s^{-1} broader than that of extended H II regions of low-emission measure (Garay and Rodriguez 1983). As can be seen in Table 10, most of the increase in the total width appears to be due to the increase in turbulent width. The turbulent velocities of $\sim 20 \text{ km s}^{-1}$ for the compact H II regions, compared to turbulent velocities of $\sim 10 \text{ km s}^{-1}$ for the extended H II regions, suggest a different dynamical stage for these nebulae. Compact H II regions could be undergoing rapid expansion motions or could be highly turbulent due to the confinement of a stellar wind by the dense neutral envelope (Reid, Myers, and Bieging 1984).

VII. CONCLUSIONS

To study the spatial and dynamical relationship between compact H II regions and OH masers, we made, using the VLA, hydrogen recombination-line observations at 15 and 22 GHz and mapped the 1.6-GHz OH maser emission toward nine regions of star formation. Our main conclusions are:

1. Compact H II regions are rarely isolated, but usually found in groups or in the vicinity of more evolved H II regions. The multiple components found in star-forming regions can be interpreted as clusters of OB stars. This was appreciated by Habing and Israel (1979), Ho and Haschick (1981), and others.

2. The OH maser emission toward star-forming regions is usually associated with the most dense and compact H II region in the complex. This association, taken together with the above conclusion, suggests that OH masers are located in dense, circumstellar envelopes surrounding very young O stars.

3. The OH maser spots are usually found on the face of the associated compact H II region. This suggests that many OH masers amplify the background emission from the compact H II region.

4. The OH masers have radial velocities that are larger than those of their associated compact H II regions. We suggest that the OH masers are part of a remnant accreting envelope that is still collapsing toward the newly formed star.

5. The average line width of the compact H II regions is $\sim 35 \text{ km s}^{-1}$, about 5 km s^{-1} broader than that of typical high-density H II regions and 10 km s^{-1} broader than that of extended, low-emission measure H II regions. The large line widths implies high turbulent velocities of $\sim 20 \text{ km s}^{-1}$. Compact H II regions are probably undergoing rapid expansion motions characteristic of the early stages in the life of an O star.

REFERENCES

- Baldwin, J. E., Harris, L. S., and Ryle, M. 1973, *Nature*, **241**, 38.
 Benson, J. M., and Johnston, K. J. 1984, *Ap. J.*, **277**, 181.
 Brocklehurst, M., and Seaton, M. J. 1972, *M.N.R.A.S.*, **157**, 179.
 Cook, A. H. 1968, *M.N.R.A.S.*, **140**, 299.
 Davies, R. D. 1974, in *IAU Symposium No. 60, Galactic Radio Astronomy*, ed. F. J. Kerr and S. C. Simonson III (Dordrecht: Reidel), p. 175.
 Downes, D., Goss, W. M., Schwartz, V. J., and Wouterloot, J. G. A. 1979, *Astr. Ap. Suppl.*, **35**, 1.
 Downes, D., Wilson, T. L., Bieging, J., and Wink, J. 1980, *Astr. Ap. Suppl.*, **40**, 379.
 Dreher, J. W., and Welch, W. J. 1981, *Ap. J.*, **245**, 857.
 Elitzur, M., and de Jong, T. 1978, *Astr. Ap.*, **67**, 323.
 Elmegreen, B. G., Genzel, R., Moran, J. M., Reid, M. J., and Walker, R. C. 1980, *Ap. J.*, **241**, 1007.
 Evans, N. J., Beckwith, S., Brown, R. L., and Gilmore, W. 1979, *Ap. J.*, **227**, 450.
 Garay, G., and Rodriguez, L. F. 1983, *Ap. J.*, **266**, 263.
 Genzel, R., Becklin, E. E., Wynn-Williams, C. G., Moran, J. M., Reid, M. J., Jaffe, D. T., and Downes, D. 1982, *Ap. J.*, **255**, 527.
 Genzel, R., and Downes, D. 1977, *Astr. Ap. Suppl.*, **30**, 145.
 Genzel, R., et al. 1981, *Ap. J.*, **247**, 1039.
 Goldreich, P., Keeley, D. A., and Kwan, J. Y. 1973, *Ap. J.*, **179**, 111.
 Gundermann, E. 1965, Ph.D. thesis, Harvard University.
 Habing, H. J., Goss, W. M., Matthews, H. E., and Winnberg, A. 1974, *Astr. Ap.*, **35**, 1.
 Habing, H. J., and Israel, F. P. 1979, *Ann. Rev. Astr. Ap.*, **17**, 345.
 Hardebeck, E. G. 1971, *Ap. J.*, **170**, 281.
 Haschick, A. D., Reid, M. J., Burke, B. F., Moran, J. M., and Miller, G. 1981, *Ap. J.*, **244**, 76.
 Ho, P. T. P., Genzel, R., and Das, A. 1983, *Ap. J.*, **266**, 596.
 Ho, P. T. P., and Haschick, A. D. 1981, *Ap. J.*, **248**, 622.
 Ho, P. T. P., Haschick, A. D., Vogel, S. N., and Wright, M. C. H. 1983, *Ap. J.*, **265**, 295.
 Hughes, V. A., and Viner, M. R. 1976, *Ap. J.*, **204**, 55.
 Humphreys, R. M. 1978, *Ap. J. Suppl.*, **38**, 309.
 Jaffe, D. T., Wilson, T. L., and Thomasson, P. 1978, *Ap. J. (Letters)*, **223**, L123.
 Larson, R. B. 1973, *Ann. Rev. Astr. Ap.*, **11**, 219.
 Larson, R. B., and Starrfield, S. 1971, *Astr. Ap.*, **13**, 190.
 Lichten, S. M., Rodriguez, L. F., and Chaisson, E. J. 1979, *Ap. J.*, **229**, 524.
 Lo, K. Y., Walker, R. C., Burke, B. F., Moran, J. M., Johnston, K. J., and Ewing, M. S. 1975, *Ap. J.*, **202**, 650.
 Martin, A. H. M. 1972, *M.N.R.A.S.*, **157**, 31.
 Martin, A. H. M., and Downes, D. 1972, *Ap. Letters*, **11**, 219.
 Matthews, H. E., Goss, W. M., Winnberg, A., and Habing, H. J. 1977, *Astr. Ap.*, **61**, 261.
 Mezger, P. G., Altenhoff, W., Schraml, J., Burke, B. F., Reifenstein, E. C., and Wilson, T. L. 1967, *Ap. J. (Letters)*, **150**, L157.
 Moran, J. M., Burke, B. F., Barrett, A. H., Rogers, A. E. E., Carter, J. C., Ball, J. A., and Cudaback, D. D. 1968, *Ap. J. (Letters)*, **152**, L97.
 Moran, J. M., Reid, M. J., Lada, C. J., Yen, J. L., Johnston, K. J., and Spencer, J. H. 1978, *Ap. J. (Letters)*, **224**, L67.
 Norris, R. P., and Booth, R. S. 1981, *M.N.R.A.S.*, **195**, 213.
 Panagia, N. 1973, *Ap. J.*, **78**, 929.
 Raimond, E., and Eliasson, B. 1969, *Ap. J.*, **155**, 817.
 Reid, M. J., Haschick, A. D., Burke, B. F., Moran, J. M., Johnston, K. J., and Swenson, G. W. 1980, *Ap. J.*, **239**, 89.
 Reid, M. J., Myers, P. C., and Bieging, J. 1984, in preparation.
 Rodriguez, L. F., Moran, J. M., Ho, P. T. P., and Gottlieb, E. W. 1980, *Ap. J.*, **235**, 845.
 Rogers, A. E. E., Moran, J. M., Crowther, P. P., Burke, B. F., Meekes, M. L., Ball, J. A., and Hyde, G. M. 1967, *Ap. J.*, **147**, 369.
 Rots, A. 1981, *A Short Guide for VLA Spectral Line Observers*, VLA memo.
 Schneps, M. H., Lane, A. P., Downes, D., Moran, J. M., Genzel, R., and Reid, M. J. 1981, *Ap. J.*, **294**, 124.
 Schraml, J., and Mezger, P. G. 1969, *Ap. J.*, **156**, 269.
 Scott, P. F. 1981, *M.N.R.A.S.*, **194**, 25.
 Thum, C., Mezger, P. G., and Pankonin, V. 1980, *Astr. Ap.*, **87**, 269.
 Turner, B. E., Balick, B., Cudaback, D. D., Heiles, C., and Boyle, R. J. 1974, *Ap. J.*, **194**, 279.
 van Gorkom, J. H., Goss, W. M., Shaver, P. A., Schwarz, V. J., and Harten, R. H. 1980, *Astr. Ap.*, **89**, 150.
 Walker, R. C., Matsakis, D. N., and Garcia-Barreto, J. A. 1982, *Ap. J.*, **255**, 128.
 Weaver, H., Williams, D. R. W., Dieter, N. H., and Lum, W. T. 1965, *Nature*, **208**, 29.
 Wink, J. E., Altenhoff, W. J., and Webster, W. J. 1975, *Astr. Ap.*, **38**, 109.
 Wynn-Williams, C. G. 1971, *M.N.R.A.S.*, **151**, 397.

GUIDO GARAY: European Southern Observatory, Karl Schwarzschild-Strasse 2, D 8046, Garching bei München, Federal Republic of Germany

JAMES M. MORAN and MARK J. REID: Center for Astrophysics, 60 Garden Street, Cambridge, MA 02138